Deconvoluting the Impacts of the Active Material Skeleton and the Inactive Phase Morphology on the Performance of Lithium Ion Battery Electrodes

Mehdi Chouchane [1,2], Alejandro A. Franco [1,2,3,4,]*

[1] Laboratoire de Réactivité et Chimie des Solides (LRCS), UMR CNRS 7314, Université de Picardie Jules Verne, Hub de l'Energie, 15 rue Baudelocque, 80039 Amiens Cedex, France.

[2] Réseau sur le Stockage Electrochimique de l'Energie (RS2E), FR CNRS 3459, Hub de l'Energie, 15 rue Baudelocque, 80039 Amiens Cedex, France

[3] ALISTORE-European Research Institute, FR CNRS 3104, Hub de l'Energie, 15 rue Baudelocque, 80039 Amiens Cedex, France.

[4] Institut Universitaire de France, 103 boulevard Saint Michel, 75005 Paris, France.

AUTHOR INFORMATION

Corresponding Author

*E-mail: alejandro.franco@u-picardie.fr

In order to extract the most capacity out of Li-ion battery (LIB) active materials, the optimization of the electrodes architectures at the mesoscale is essential. This work focuses on the morphology of the inactive phase (carbon additives and binder) through a 3-D modeling approach based on stochastic generation with realistic $LiNi_{1/3}Mn_{1/3}Co_{1/3}O_2$ particle size distributions. It was found that having the inactive phase as a film spread on the active material results in poorer performance in part due to the loss of active surface area when compared to an agglomerates morphology.
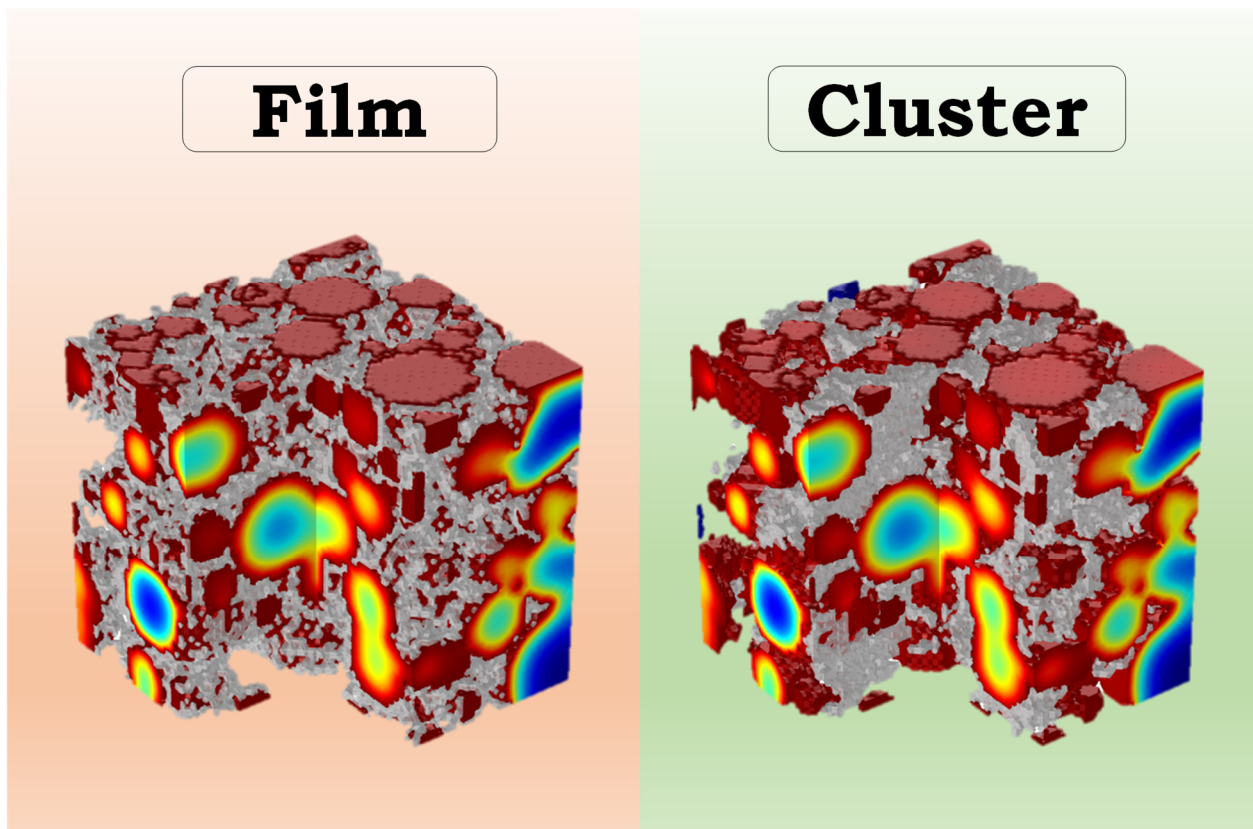
3-D computational modeling using continuum approaches supported on Finite Element or Volume Methods in the LIB field has known exciting new developments in the recent years. Whether it is the dynamic embedding of mechanics through stress during discharge,[1] or the tremendous progress in the spatial resolution of the simulation supported by imaging,[2] 3-D modeling can assist in the optimization of the electrodes architectures. For instance the manufacturing process can be optimized through the slurry casting and drying,[3] the calendering,[4,5] and the design of the components of the electrode can be supported by modeling, *i.e.* the active material (AM) can be optimized through its microstructure, size or surface[6,7], and the inactive phase through its composition and morphology.[8]

In the 3D-resolved computational models, the inactive phase (carbon additives and binder) is considered as a single phase as carbon and binder domains (CBD) to decrease the complexity of the system. In recent years, a growing interest has been observed for CBD, with Danner *et al.* in late 2016 who investigated the impact of a poorly connected CBD region on the performance of a thick cell.[9] Then, in 2019 an article published by us was addressing the physics that should be applied to the inactive phase by comparing different hypotheses.[10] More recently, Lu *et al.* reported a 3-D model where the microstructure of the CBD was explicitly resolved.[2] Yet, only Mistry *et al.* focused on the morphology of the inactive phase, through a screening of different parameters to determine effective properties of stochastically generated 3-D structures that were fed to a 1-D model.[11] Their approach allowed them to build 2-D classification graphs for the limitations of the system, but they used homogenized values for structural parameters and they could not capture the causal link at the particle level. It transpires that with the recent development

of the field, it is necessary to investigate the influence of the CBD morphology on the electrodes performance based on 3D-resolved computational models.

To study the impact of the morphology of the CBD on the electrochemical behavior of an electrode, the system chosen in this work is a half-cell electrode with $LiNi_{1/3}Mn_{1/3}Co_{1/3}O_2$ (NMC) with a homogeneous separator that can be visualized in **Figure S1** in the Supporting Information The electrodes are $40\times40\times60$ µm^3 and have an NMC:CBD weight ratio of 94:6. It is assumed that 50% of the CBD is composed of micropores where the Li^+ can diffuse.[12] The positive electrodes arose from stochastic generation, as illustrated in **Figure 1a**, using an *in house* library of NMC particles obtained from tomography data for the AM skeleton. Two different types were generated, one with 33% of porosity (25% in the bulk and 8% in the CBD micropores) called hereafter High Porosity -HP- electrode, and one with with 25% of porosity (15% in the bulk and 10% in the CBD micropores) called hereafter Low Porosity (LP) electrode. These two conditions were repeated twice for a total of four NMC skeletons (HP-1, HP-2, LP-1, LP-2) to take into account the stochastic nature of the generation. Moreover, our INNOV algorithm that can control the morphology of the CBD was used to add the CBD as a film or as an aggregate.[13] For a given NMC skeleton HP-1, arose two electrodes with CBD as film (HP-1$_{film-1}$, HP-1$_{film-2}$) and two with CBD as aggregates (HP-1$_{agg-1}$, HP-1$_{agg-2}$). The difference between the two configurations can be seen in **Figure 1(b,c)** for a slice of respectively HP-1$_{film-1}$ and HP-1$_{agg-1}$. Finally, the electrode mesostructures were meshed using INNOV[13,14] (with all the NMC particles individually identified), and fed to a Newman-based[15,16] 3-D model used in our previous studies,[5,17] to simulate a discharge at rate of 3C.
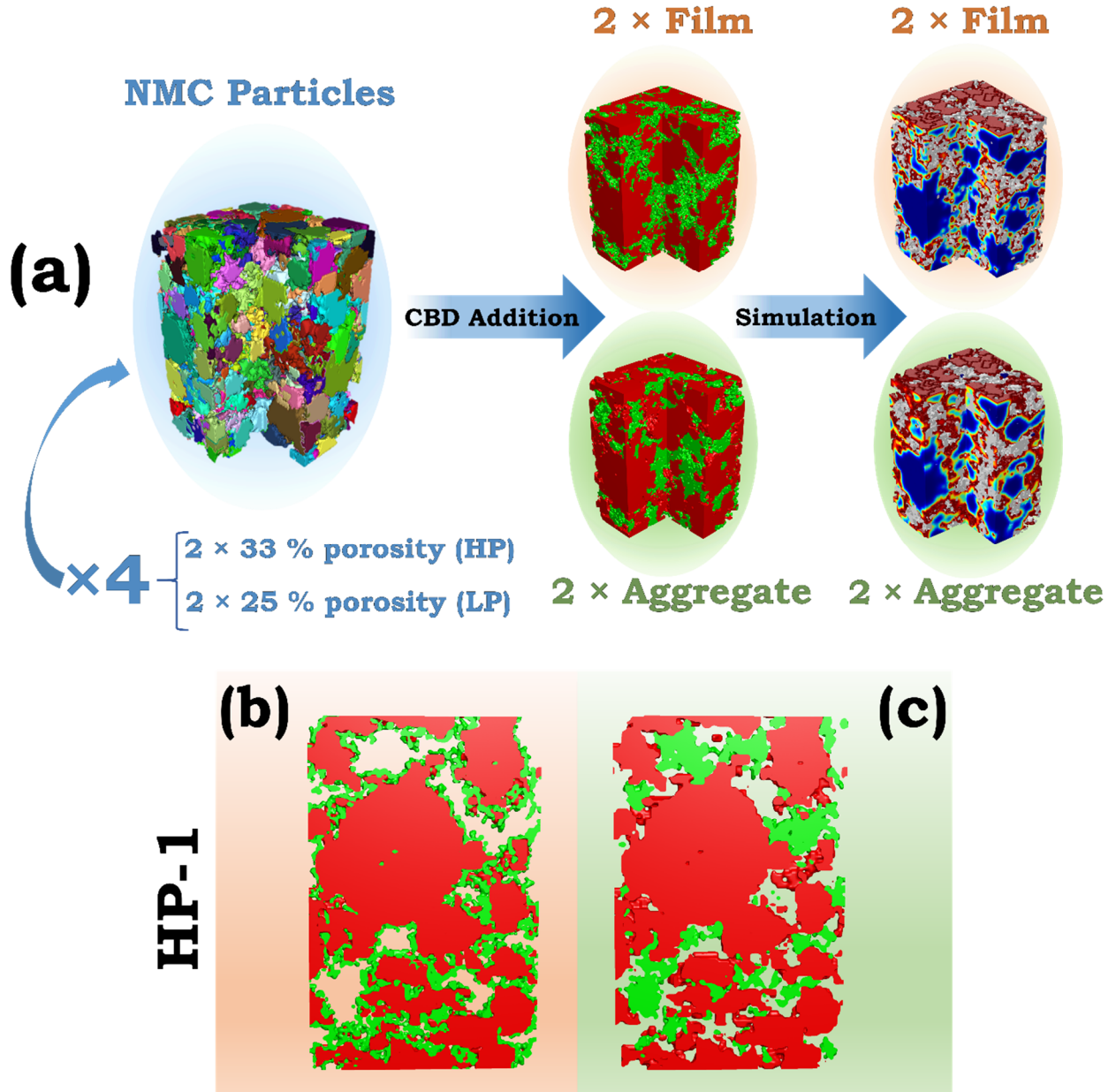
Figure 1. (a) The workflow of the study with the generation of the four NMC particles structures, two with high porosity (HP) and two with low porosity (LP), followed by the stochastic addition of CBD twice as film and twice as aggregates and finally the 3-D electrochemical modeling. Slices of two electrodes with high porosity sharing the same NMC particles but different CBD with (b) the film one and (c) the aggregate one.

In **Figure 2a**, the discharge curves obtained for the four different cases are represented with the dispersion related to the stochastic nature of the electrode generation. For a given condition HP_{agg}, the results obtained with the electrode mesostructures with the same NMC skeleton (*i.e.* $HP-1_{agg-1}$ with $HP-1_{agg-2}$, and $HP-2_{agg-1}$ with $HP-2_{agg-2}$) have been averaged so the light green region is the area between the two discharge curves representing $HP-1_{agg}$ and $HP-2_{agg}$ mesostructures. In other words, the colored regions represent the impact of the NMC skeleton on the behavior of the half-cell. It appears that differences from three distinct origins can be observed. Firstly, the impact of the CBD through the aggregates morphologies that perform better in terms of specific capacity with regards to the film configurations. Secondly, the significant variations due to the NMC skeleton are visible from the colored areas: for instance for the LP_{film} case the specific capacities range from 41 to 54 $mAh.g^{-1}_{NMC}$. It is noteworthy that the dispersion due to the CBD addition (between $HP-1_{agg-1}$ and $HP-1_{agg-2}$ or $LP-2_{film-1}$ and $LP-2_{film-2}$ for instance) is almost negligible, which proves that more repetitions of the CBD addition step in the electrode stochastic generation are not necessary. Lastly, for the low porosity cases, for a given CBD morphology the specific capacities are systematically lower than the high porosity cases.

These macroscale discrepancies arose from lower scale differences, and in that regard 3-D modeling is a powerful tool to access observables (difficult to obtain experimentally) at any location and time during the discharge. The distribution of the state of lithiation (SoL), *i.e.* $[Li]_{NMC}$ /$[Li]_{NMC,max}$, is represented in **Figure 2(b,c)** for HP-1 at the end of discharge for respectively the film and aggregates CBD. Despite having the same NMC particles, the SoL is not distributed in the same manner at the electrode level. However, the solid diffusion is limiting in the two cases with the cores of the large NMC particles being almost unutilized during the discharge.

The impact of the CBD morphology also translates at the particle level by a more heterogeneous distribution of the SoL as seen in **Figure 2(d,e)**. Indeed for the film case (**Figure 2d**), due to the loss of active surface area because of NMC/CBD contacts (represented by the black wireframe), the Li^+ will be intercalated at few "hotspots" leading to locally high SoL while for the CBD as aggregates (**Figure 2e**), the distribution is more homogeneous because of the larger active surface area available.
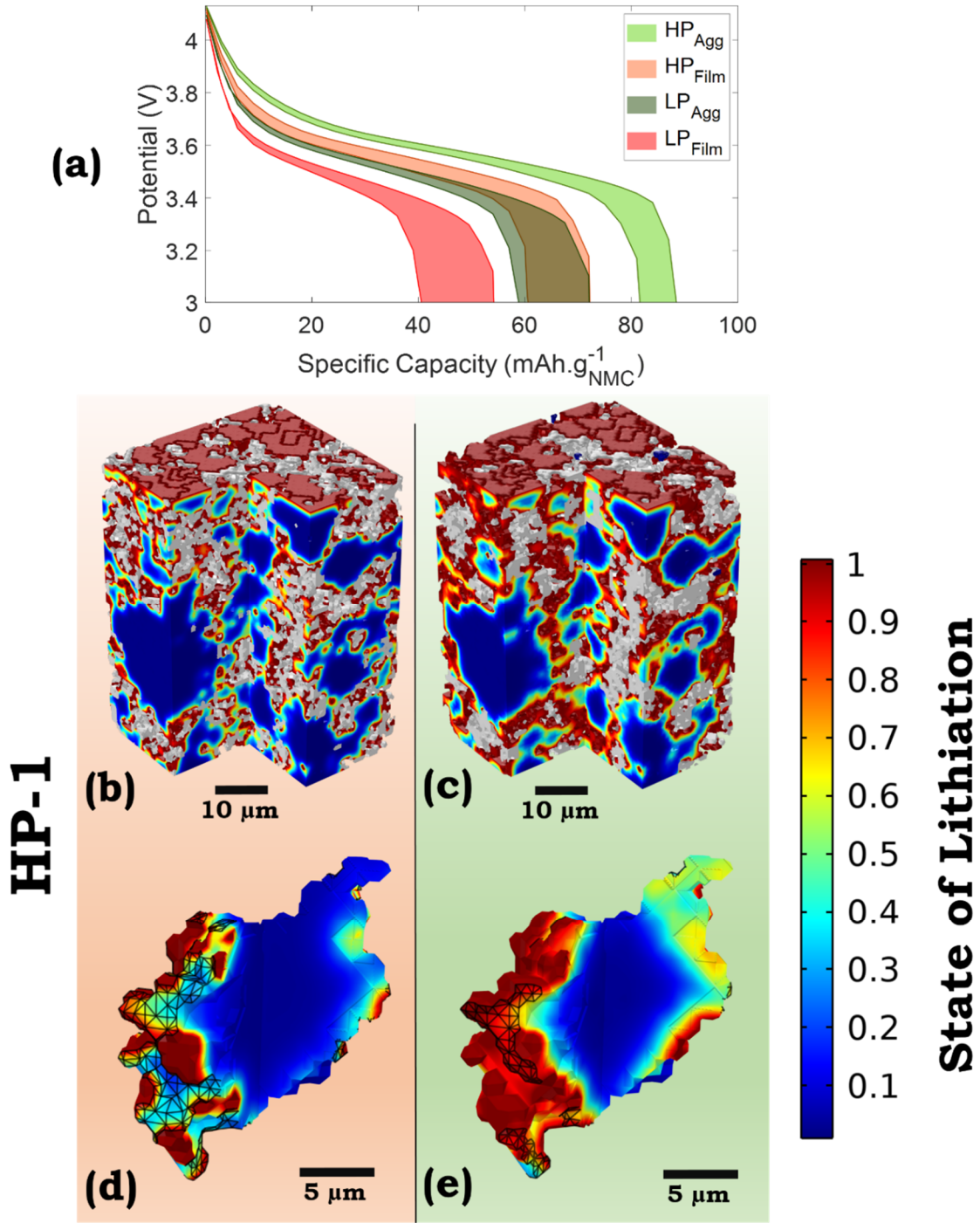
Figure 2. (a) Discharge curves at a C-rate of 3C with the dispersion due to the NMC skeleton for each condition. The spatial distribution of the SoL at the end of discharge with the CBD in grey is reported for (b) HP-1$_{film-1}$ and (c) HP-1$_{agg-1}$, and also at the particle level with the surface of contact with CBD in black wireframe represented in (d) and (e).

As seen previously, the lower porosity has a poorer rate capability than the higher porosity. Indeed, when the porosity is decreased, both the electronic conductivity and the tortuosity factor in the electrolyte will increase, the latter being detrimental to the performance of the battery. For a given AM and electrode composition, finding the optimal porosity is a trade-off between the ionic and electronic transport limitations. Here the effective electronic conductivity of the electrodes have been characterized using GeoDict® and the tortuosity factors in the electrolyte (taking into account the micropores in the CBD) have been determined thanks to TauFactor (**Figure 3a**).[18]

The film morphology exhibits a lower effective electronic conductivity with regards to the aggregates one. The difference is particularly significant for the high porosity, since the solid contact will be improved, as the porosity gets lower. This trend is not in agreement with the findings of Mistry *et al.*[11], who found that the film configuration had a higher effective electronic conductivity. This discrepancy can be explained by the difference in the algorithm used for the stochastic generation of CBD. Indeed, the present algorithm allows to have more pronounced differences at the electrode scale while the one used by Mistry *et al.* has a higher impact at the microscale.

Moreover, in our study the tortuosity factor τ_{liq} is higher for LP mesostructures and for the CBD as a film. Indeed, with a higher porosity, there are more pathways available for the Li^+, and with CBD as aggregates, even though some pores might be fully clogged, large pores almost not clogged with CBD will remain to ensure a proper transport of the ions. Yet, the difference of the profile of concentration of Li^+ at the end of discharge along the thickness of the electrode is almost negligible between HP-1$_{agg}$ and HP-1$_{film}$, and between LP-1$_{agg}$ and LP-1$_{film}$ according to **Figure**

3b. The gradient of concentration is driven by the NMC skeleton more than the CBD morphology, as LP-1 demonstrates a steeper gradient of concentration in the electrolyte than HP-1.

From **Figure 3(a,b)**, it comes that HP_{agg} has a satisfactory effective electronic conductivity and a mild $[Li^+]_{electrolyte}$ gradient. If between the effective electronic conductivity of the electrode κ_{eff} and the electrolyte ionic conductivity κ_{ion} one is an order of magnitude higher than the other, then the limitation of the latter can be neglected. Here, κ_{ion} is a function of the electrolyte concentration[19], and in the range of values of $[Li^+]_{electrolyte}$, κ_{ion} is around 0.5 S.m^{-1}. For HP_{agg}, κ_{eff} ranges from 1.27 S.m^{-1} to 3.78 S.m^{-1}, hence a dual limitation from the electronic and ionic transports. While for LP_{agg}, κ_{eff} and τ_{liq} are higher, hence a stronger ionic limitation visible from the gradient of $[Li^+]_{electrolyte}$ in **Figure 3b**.

These observations will impact the lithiation process during the discharge, as illustrated by the lithiation change, *i.e.* the difference in SoL, between different depths of discharge (DoD) in **Figure 3(c-h)**. This observable highlights how fast each NMC particles are lithiated during a given period, here during the second and last quarters of the discharge. For HP-1$_{agg-1}$ in **Figure 3(c,d)**, since both limitations are not negligible, we do not obtain a clear trend where the top or bottom regions are favored, instead the lithiation change is more or less homogeneous.

Now, if we take the example of an electrode with more a pronounced ionic transport limitation, *i.e.* LP-1$_{agg-1}$, it is clear from **Figure 3e** that during the second quarter of discharge, the region closer to the separator is getting lithiated faster than the rest of the electrode, regardless of the size of the particles. The NMC particles in this region will reach a concentration close to the maximum one, entailing a decay of the lithiation speed in the last quarter of discharge as evidenced in **Figure 3f**. Interestingly, LP-1$_{film-1}$, that has the same NMC skeleton as LP-1$_{agg-1}$, hence a similar $[Li^+]_{electrolyte}$ gradient, demonstrates a milder gradient of lithiation change (**Figure 3(g,h)**). The

lithiation process is more homogeneous because the film configuration results in a lower κ_{eff} (2.03 S.m^{-1} vs 7.08 S.m^{-1}), entailing a higher electronic limitation that will compete with the ionic transport limitation.
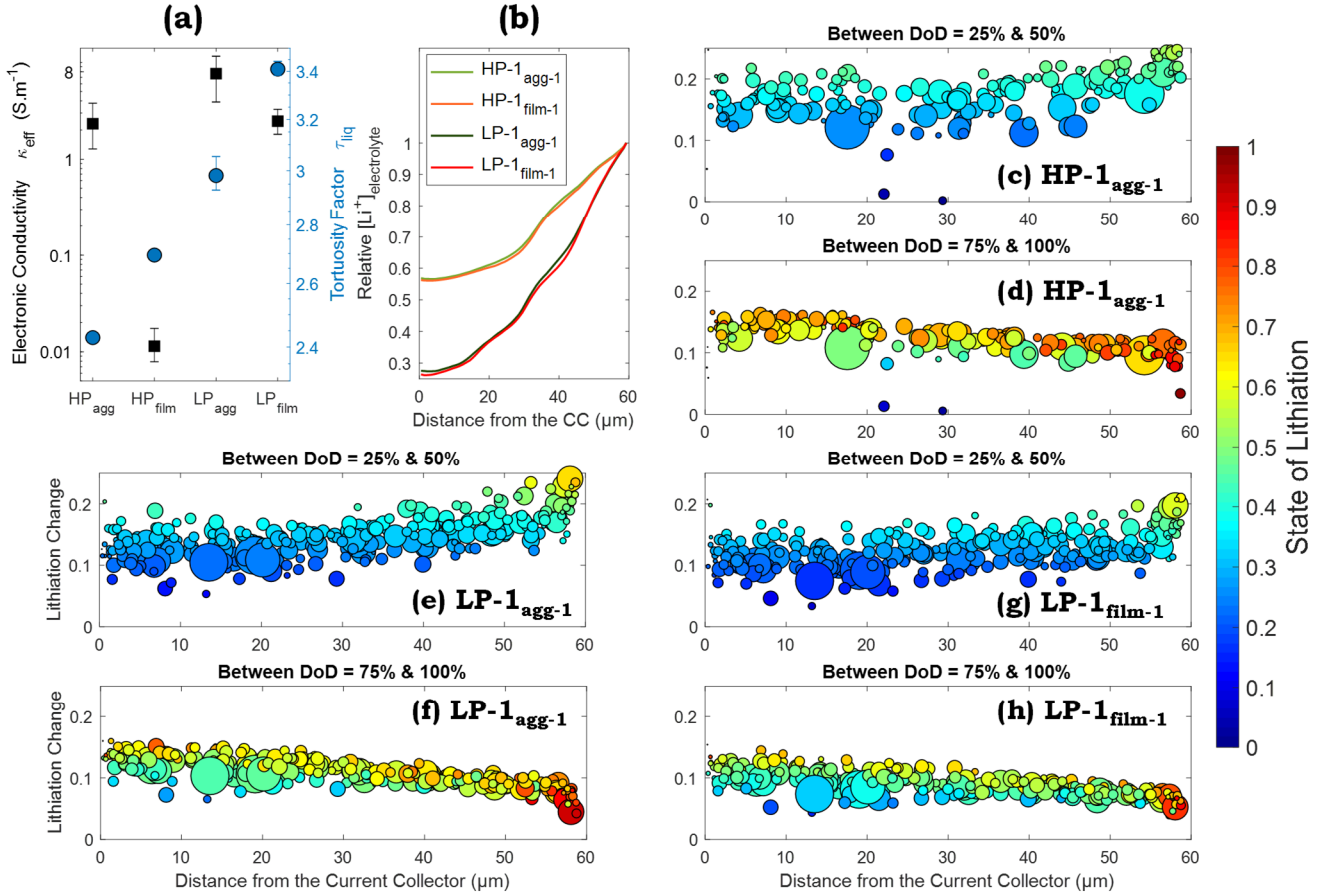

Figure 3. (a) Effective electronic conductivities (■) and tortuosity factors (●) of the electrolyte (bulk + CBD micropores) averaged for the different conditions. (b) Normalized electrolyte concentration in Li$^+$ ([Li$^+$] / [Li$^+$]$_{max}$) as a function of the distance from the current collector at the end of discharge for four conditions. (c-h) The lithiation change, *i.e.* the difference in lithiation state between two depths of discharge (DoD) as a function of the distance from the current collector. The color indicates the SoL of the particles at the intermediate DoD, *i.e.*37.5% and 87.5%, and the size of the disks is proportional to the volume of the NMC particles.

As highlighted in **Figure 2(b-e)**, the CBD will not only impact in the electronic percolation, but also through the loss of active surface area where the Li^+ can react. Due to the limited surface area in the film cases, the appearance of "hotspots" for the lithiation of the NMC was demonstrated at the particle level. The resulting higher heterogeneity is also noticeable at the electrode level with the average $[Li]_{NMC}$ gradient reported as a function of the DoD in **Figure 4(a,b)**. At first the gradient is increasing until DoD = 50% because the simulations start from a fully delithiated NMC, so the lithiation of the surface of the particles will drastically increase the gradient of concentration. Then, the average gradient drops thanks to solid diffusion softening the intra-particles gradient and to the lithiation process happening at places less favorable because of the higher SoL of the more favorable active surface regions. The average gradients for the LP cases (**Figure 4b**) are systematically higher for a given CBD morphology than the HP ones (**Figure 4a**) because of a poorer electrode utilization in the LP cases as illustrated by the lower specific capacity in discharge (**Figure 2a**). From the study of Mistry *et al.,*[11] they had also identified the loss of active surface area as one of the main factor to the drop of capacity in the electrode with CBD as film.

To go further in the analysis, it is possible with this workflow, for a given NMC skeleton, to compare between NMC particles with CBD as film or as aggregates. The difference in SoL as a function of the difference in relative surface area (active surface area / (active surface area + NMC/CBD surface area)) is represented for HP-1$_{agg-1}$ - HP-1$_{film-1}$ in **Figure 4(c,d)**, and in **Figure 4(e,f)** for LP-1$_{agg-1}$ - LP-1$_{film-1}$. In both cases, there is a clear relationship between the difference in SoL and the difference in active surface area, almost linear for DoD = 25 % in **Figure 4(d,f)**. The more active surface area is available, the higher will be the SoL of the particles. Moreover, this

difference increases during the discharge as seen **Figure 4(e,g)**, with the slope coefficient (based on a linear fitting) increasing by ca. 75% between DoD = 25% and DoD = 100%.
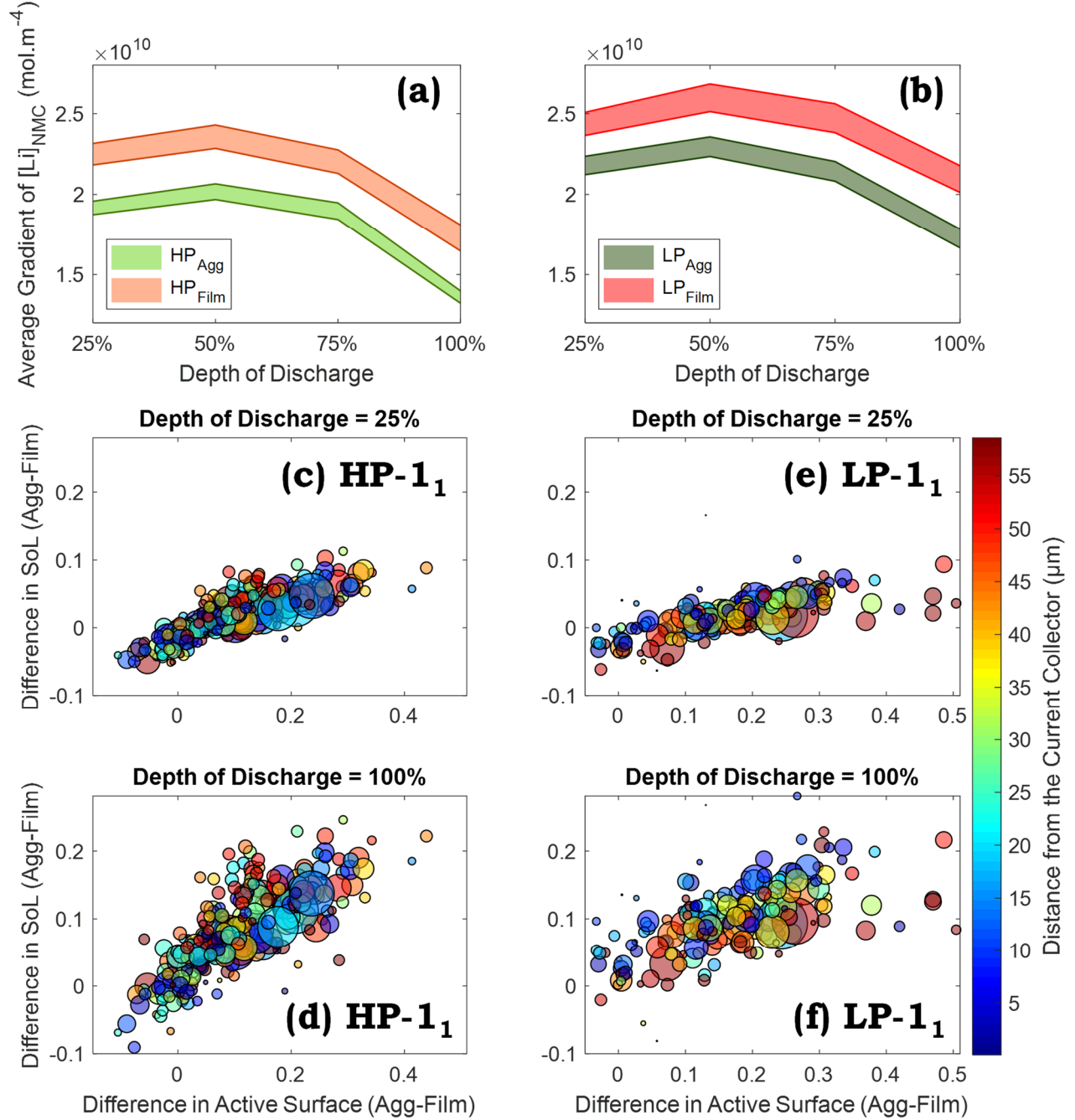

Figure 4. The average gradient of Li in the NMC particles at different DoD for the (a) HP and (b) LP structures. (c-f) The difference in the state of lithiation versus the difference in relative active

surface area (active surface area / (active surface area + NMC/CBD surface area)) for each of the particles in the electrode mesostructures with CBD as agglomerate and film.

For the LP-1 (**Figure 4f**), it is noteworthy that between DoD = 25% and DoD = 100%, most of the particles demonstrating the highest SoL difference for a given difference in active surface area are located close to the current collector, while it was not the case at DoD = 25% (**Figure 4e**). It can be explained by the higher lithiation change this region will undergo at the end of discharge due to ionic limitation as demonstrated in **Figure 3(e-h)**.

This investigation allowed deconvoluting the influence of the NMC skeleton from the impact of the CBD morphology on the electrochemical behavior of the electrode. While the NMC has a higher impact on the electrolyte concentration gradient, at high porosities the CBD morphology will drive the effective electronic conductivity of the electrode. Furthermore, the CBD morphology will play a significant role on the lithiation process that will be more homogeneous in the case of an aggregate-like configuration because of the larger active surface area for the Li^+ to react. A heterogeneous lithiation process entails a higher utilization of given regions of the electrode, thus a risk of cracking due to the stress from the deep variations in SoL. It results that having control at the experimental level over the CBD morphology would be highly beneficial to the performance of a LIB cell, and it is a subject not so much addressed in the experimental literature.

ASSOCIATED CONTENT

AUTHOR INFORMATION

Corresponding Author

*E-mail: alejandro.franco@u-picardie.fr

ABBREVIATIONS

AM, Active Material; CBD, Carbon Binder Domains; DoD, Depth of Discharge; LIB, Lithium-ion Battery; NMC, $LiNi_{1/3}Mn_{1/3}Co_{1/3}O_2$; SoL, State of Lithiation.

REFERENCES

(1)   Ferraro, M. E.; Trembacki, B. L.; Brunini, V. E.; Noble, D. R.; Roberts, S. A. Electrode Mesoscale as a Collection of Particles: Coupled Electrochemical and Mechanical Analysis of NMC Cathodes. *Journal of The Electrochemical Society* **2020**, *167* (1), 013543. https://doi.org/10.1149/1945-7111/ab632b.

(2)   Lu, X.; Bertei, A.; Finegan, D. P.; Tan, C.; Daemi, S. R.; Weaving, J. S.; Regan, K. B. O.; Heenan, T. M. M.; Hinds, G.; Kendrick, E.; Brett, D. J. L.; Shearing, P. R. 3D Microstructure Design of Lithium-Ion Battery Electrodes Assisted by X-Ray Nano-Computed Tomography and Modelling. *Nature Communications* **2020**, *11* (2079), 1–13. https://doi.org/10.1038/s41467-020-15811-x.

(3)   Lombardo, T.; Ngandjong, A. C.; Belhcen, A.; Franco, A. A. Carbon-Binder Migration: A Three-Dimensional Drying Model for Lithium-Ion Battery Electrodes. *Energy Storage Materials* **2021**, *43*, 337–347. https://doi.org/10.1016/j.ensm.2021.09.015.

(4)   Lu, X.; Daemi, S. R.; Bertei, A.; Kok, M. D. R.; O'Regan, K. B.; Rasha, L.; Park, J.; Hinds, G.; Kendrick, E.; Brett, D. J. L.; Shearing, P. R. Microstructural Evolution of Battery Electrodes During Calendering. *Joule* **2020**, *4* (12), 2746–2768. https://doi.org/10.1016/j.joule.2020.10.010.

(5)   Ngandjong, A. C.; Lombardo, T.; Primo, E. N.; Chouchane, M.; Shodiev, A.; Arcelus, O.; Franco, A. A. Investigating Electrode Calendering and Its Impact on Electrochemical Performance by Means of a New Discrete Element Method Model: Towards a Digital Twin of Li-Ion Battery Manufacturing. *Journal of Power Sources* **2021**, *485*, 229320. https://doi.org/10.1016/j.jpowsour.2020.229320.

(6)   Lu, X.; Zhang, X.; Tan, C.; Heenan, T. M. M.; Lagnoni, M.; O'Regan, K.; Daemi, S.; Bertei, A.; Jones, H. G.; Hinds, G.; Park, J.; Kendrick, E.; Brett, D. J. L.; Shearing, P. R. Multi-Length Scale Microstructural Design of Lithium-Ion Battery Electrodes for Improved Discharge Rate Performance. *Energy Environ. Sci.* **2021**, 10.1039.D1EE01388B. https://doi.org/10.1039/D1EE01388B.

(7)   Nelson, G. J.; Ausderau, L. J.; Shin, S.; Buckley, J. R.; Mistry, A.; Mukherjee, P. P.; De Andrade, V. Transport-Geometry Interactions in Li-Ion Cathode Materials Imaged Using X-Ray Nanotomography. *Journal of The Electrochemical Society* **2017**, *164* (7), A1412–A1424. https://doi.org/10.1149/2.0261707jes.

(8)   Mistry, A. N.; Mukherjee, P. P. Probing Spatial Coupling of Resistive Modes in Porous Intercalation Electrodes through Impedance Spectroscopy. *Phys. Chem. Chem. Phys.* **2019**, *21* (7), 3805–3813. https://doi.org/10.1039/C8CP05109G.

(9)   Danner, T.; Singh, M.; Hein, S.; Kaiser, J.; Hahn, H.; Latz, A. Thick Electrodes for Li-Ion Batteries: A Model Based Analysis. *Journal of Power Sources* **2016**, *334*, 191–201. https://doi.org/10.1016/j.jpowsour.2016.09.143.

(10)   Chouchane, M.; Rucci, A.; Lombardo, T.; Ngandjong, A. C.; Franco, A. A. Lithium Ion Battery Electrodes Predicted from Manufacturing Simulations: Assessing the Impact of the Carbon-Binder Spatial Location on the Electrochemical Performance. *Journal of Power Sources* **2019**, *444*, 227285. https://doi.org/10.1016/j.jpowsour.2019.227285.

(11)   Mistry, A. N.; Smith, K.; Mukherjee, P. P. Secondary-Phase Stochastics in Lithium-Ion Battery Electrodes. *ACS Applied Materials and Interfaces* **2018**, *10* (7), 6317–6326. https://doi.org/10.1021/acsami.7b17771.

(12)   Zielke, L.; Hutzenlaub, T.; Wheeler, D. R.; Chao, C. W.; Manke, I.; Hilger, A.; Paust, N.; Zengerle, R.; Thiele, S. Three-Phase Multiscale Modeling of a LiCoO2 Cathode: Combining the Advantages of FIB-SEM Imaging and X-Ray Tomography. *Advanced Energy Materials* **2015**, *5* (5), 1–8. https://doi.org/10.1002/aenm.201401612.

(13)   Chouchane, M.; Franco, A. A. An Invitation to Engage with Computational Modeling: User-Friendly Tool for In Silico Battery Component Generation and Meshing. *Batteries & Supercaps* **2021**, *4*, 1451–1456. https://doi.org/10.1002/batt.202100096.

(14)   Chouchane, M.; Rucci, A.; Franco, A. A. A Versatile and Efficient Voxelization-Based Meshing Algorithm of Multiple Phases. *ACS Omega* **2019**, *4* (6), 11141–11144. https://doi.org/10.1021/acsomega.9b01279.

(15)   Doyle, M.; Fuller, T. F.; Newman, J. Modeling of Galvanostatic Charge and Discharge of the Lithium/Polymer/Insertion Cell. *Journal of The Electrochemical Society* **1993**, *140* (6), 1526. https://doi.org/10.1149/1.2221597.

(16)   Doyle, M.; Newman, J.; Gozdz, A. S.; Schmutz, C. N.; Tarascon, J. Comparison of Modeling Predictions with Experimental Data from Plastic Lithium Ion Cells. *Journal of The Electrochemical Society* **1996**, *143* (6), 1890. https://doi.org/10.1149/1.1836921.

(17)   Chouchane, M.; Primo, E. N.; Franco, A. A. Mesoscale Effects in the Extraction of the Solid-State Lithium Diffusion Coefficient Values of Battery Active Materials: Physical Insights from 3D Modeling. *The Journal of Physical Chemistry Letters* **2020**, *11* (7), 2775–2780. https://doi.org/10.1021/acs.jpclett.0c00517.

(18)   Cooper, S. J.; Bertei, A.; Shearing, P. R.; Kilner, J. A.; Brandon, N. P. TauFactor: An Open-Source Application for Calculating Tortuosity Factors from Tomographic Data. *SoftwareX* **2016**, *5*, 203–210. https://doi.org/10.1016/j.softx.2016.09.002.

(19)   Smith, K. A.; Rahn, C. D.; Wang, C.-Y. Control Oriented 1D Electrochemical Model of Lithium Ion Battery. *Energy Conversion and Management* **2007**, *48* (9), 2565–2578. https://doi.org/10.1016/j.enconman.2007.03.015.